Vibration and damping analysis of a thin finite-size microperforated plate

Lucie Gallerand, Mathias Legrand, Thomas Dupont, Philippe Leclaire

▶ To cite this version:

Lucie Gallerand, Mathias Legrand, Thomas Dupont, Philippe Leclaire. Vibration and damping analysis of a thin finite-size microperforated plate. Journal of Sound and Vibration, 2022, 541, pp.117295. ⟨10.1016/j.jsv.2022.117295⟩. ⟨hal-03634548v2⟩

HAL Id: hal-03634548
https://hal.science/hal-03634548v2

Submitted on 13 Sep 2022

Vibration and damping analysis of a thin finite-size microperforated plate

Lucie Gallerand[a], Mathias Legrand[b], Thomas Dupont[a], Philippe Leclaire[c]

[a]*Department of Mechanical Engineering, École de technologie supérieure, Montréal, Canada*
[b]*Department of Mechanical Engineering, McGill University, Montréal, Canada*
[c]*DRIVE EA1859, Université de Bourgogne Franche-Comté, ISAT, Nevers, France*

Microperforated plates (MPP) are commonly used to absorb acoustic waves in sound control technologies. However, less is known concerning the added damping exhibited by thin finite-size MPPs. This added damping effect is known to be induced by viscous and thermal exchanges in the boundary layers near the fluid-solid interface of the perforations, which results in energy dissipation. The present work actually shows that MPPs can feature a significant added viscous damping, especially at low frequencies of vibration. An analytical approach based on an alternative form of the Biot theory for finite size porous plates is developed. Parametric studies highlight the existence of a characteristic damping frequency at which the added damping of the perforations reaches a maximum. For specified boundary conditions, the damping level can be maximized by adjusting the geometrical parameters of the perforations (diameter, perforation ratio) so that the resonance frequency of the plate coincides with the characteristic damping frequency. The damping reaches a maximum at a particular frequency, and is also effective over a non-negligible bandwidth. Formulations on the mass density and Young's modulus as a function of the perforation ratio are provided to address the sensitivity of mass and stiffness to the microperforations. The structural damping capabilities of MPPs are validated by measurements on finite size MPPs which confirm the significant damping increase in the low-frequency range.

Keywords: Microperforated plate — Vibration analysis — Added viscous damping — Fluid-solid interactions

---

Contents

Email addresses: `lucie.gallerand.1@ens.etsmtl.ca` (Lucie Gallerand), `mathias.legrand@mcgill.ca` (Mathias Legrand), `thomas.dupont@etsmtl.ca` (Thomas Dupont), `philippe.leclaire@u-bourgogne.fr` (Philippe Leclaire)

Nomenclature

Geometric constants

d	diameter of perforation (mm)
h	plate or MPP thickness (mm)
L_x	plate or MPP length in x direction (mm)
L_y	plate or MPP length in y direction (mm)

Macroscopic parameters

α_∞	tortuosity
ϕ	perforation ratio
σ	fluid flow resistivity ($\mathrm{N\,s\,m^{-4}}$)
b_f	Biot's friction coefficient ($\mathrm{N\,s\,m^{-4}}$)
f_Biot	Biot's characteristic frequency (Hz)

Mechanical parameters

α	Biot's elastic coupling coefficient
η	loss factor
η_s	isotropic structural loss factor
η_{mn}	loss factor of mode mn
μ_f	fluid dynamic viscoelasticity ($\mathrm{kg\,m^{-1}\,s^{-1}}$)
ν_0	Poisson's coefficient
ρ	plate effective density ($\mathrm{kg\,m^{-3}}$)
ρ_f	fluid density ($\mathrm{kg\,m^{-3}}$)
ρ_s	stucture density ($\mathrm{kg\,m^{-3}}$)
ζ	modal damping ratio
ζ_{mn}	modal damping ratio of mode mn
D	bending stiffness ($\mathrm{GPa\,mm^3}$)
E	Young's modulus (GPa)
K_f	fluid bulk modulus (kPa)
M_f	Biot's elastic coefficient ($\mathrm{N\,m^{-2}}$)

Other parameters

λ	eigenvalue
λ_{mn}	eigenvalue of mode mn
β	real part of λ
β_{mn}	real part of λ_{mn}
γ	imaginary part of λ ($\mathrm{rad\,s^{-1}}$)
γ_{mn}	imaginary part of λ_{mn} ($\mathrm{rad\,s^{-1}}$)
ω	angular frequency ($\mathrm{rad\,s^{-1}}$)
ω_{mn}	angular undamped frequency of mode mn ($\mathrm{rad\,s^{-1}}$)
N	number of degrees-of-freedom (dof) in plate discretization
$\Psi_{mn}(x,y)$	modal shape of mode mn
$w_\mathrm{s}(x,y,t)$	solid motion
$w(x,y,t)$	fluid-solid relative motion

1. Introduction

Microperforated plates (MPP) are simple, lightweight structures already used in various noise control applications, such as acoustic coatings in flow ducts [41] or cooling systems for turbines. These structures can also be used to reduce noise in hostile environments, such as nuclear engines and reactors [40], launcher fairings [32]. Various microperforated materials have been proposed [13, 25, 30] and applied to create comfortable spaces, rooms, and environments [1]. These structures are known to dissipate acoustic energy as heat via visco-thermal effects if the size of the perforations is of the same order as the size of the viscous and thermal boundary layers [4].

Various theories and linear models for microperforated panels are now available. One of the earliest studies of the acoustic behaviour of microperforated panels introduced a model with distributed Helmholtz resonators [17] and was followed by similar work using the analogy between mechanical and electrical systems [29]. The study of MPP based on sound propagation in thin tubes of small sections was also proposed via simplified Kirchhoff equations by Maa [26, 27] who established a simple formulation for the acoustic impedance of an MPP. From Maa's works, it was shown that the MPP can be optimized to induce maximum acoustic absorption. For this purpose, the maximum absorption was obtained as a function of the diameter of the perforations and their distribution over the structure [12].

MPPs have also been investigated in vibroacoustics, mainly via the electrical analogy approach, until the 2000s [20]. This vibroacoustic approach was notably used by Dupont *et al.* [15] to characterize the acoustic transparency factor for an MPP. Takahashi and Tanaka [37] also proposed to study the vibroacoustics of MPPs and introduced the notion of relative velocity. They highlighted the correlation between the size of the perforations and the acoustic absorption efficiency of the MPP. This work was extended by Lee *et al.* [24], who were able to demonstrate that the vibrations of MPPs strongly affected their acoustic response, as they resulted in additional energy dissipation. Later, Lee *et al.* [23] proposed to study sound absorption of flexible curved micro-perforated panels, backed by an air cavity, using an electro-acoustic analogy. They observed that microperforations could induce an additional damping on structural vibration responses. However, the magnitude of this added damping and its sensitivity to geometric parameters have not yet been explored. Other approaches, such as the modal approach, had also been proposed by Bravo *et al.* [9] to study the sound absorption and transmission loss of a finite microperforated panel. They had deduced that MPPs induced a change in sound absorption. In another study, they had used the modal approach to determine the influence of vibration on the acoustic absorption and transmission loss of a finite size microperforated panel [10]. Their work had shown that the relative velocity between the structure and the surrounding fluid should be considered when studying the vibrations of the MPP. They concluded that considering the MPP vibration generated an additional absorption peak. In addition, the geometric and mechanical parameters of thin MPPs could be modified to satisfy a required sound absorption. Another study, carried out over a wide range of frequencies, had been proposed to determine the influence of microperforation on a honeycomb structure [36]. The mechanisms involved in microperforations were modelled as a mass-spring-damping system. The shape of the structure as well as the frequency band considered did not allow obtaining conclusive results concerning the added damping for the microperforations. Parametric studies have also been performed to better understand the effects of perforations on the vibrations of microperforated plates. To this end, Putra and Thompson [35] studied the influence of the porosity and the diameter of the perforations on the efficiency of the acoustic radiation. Moreover, the vibration characteristics of microperforated plates (natural frequencies and damping) for different sizes and number of perforations has been studied [18]. They have shown that in a heavy fluid, the perforations increased the damping of the structure. Other parametric studies considering the influence of the diameter of the perforations and their number have been performed, highlighting the influence of the position of the perforations on the dynamics of the plate [33, 34].

In parallel to the models developed for the MPPs, work on the vibratory response of porous plates has been carried out. Indeed, from the theory of thin rectangular finite plates, an analytical model based on the stress-strain relation of Biot [5, 6] has been developed by Theodorakopoulos and Beskos for porous materials [38]. Using an alternative form of Biot's poroelasticity equations and an additional simplifying assumption, Leclaire *et al.* [21, 22] were able to propose a simpler model in the form of two coupled partial differential equations governing the dynamics of the porous plate. They had shown that porous plates induce an added viscous damping and a maximum damping condition involving porous geometric parameters were given [21]. The fluid-structure interaction and the acoustic radiation were then implemented by Aygun *et al.* [3].

Furthermore, for a sufficiently rigid structure, it was proposed by Atalla and Sgard [2] to study the MPP as porous structure using an equivalent fluid model based on the Johnson-Allard approach for porous materials. Under simplifying assumptions (rigid frame, small plate thickness with respect to any acoustic wavelength), the Biot parameters used for porous structures could also be defined for MPPs and a length correction factor allowing considering the radiation induced by the distortion of the fluid at the end of the perforations [2, 19].

The addition of microperforations on a plate has an influence on the sound absorption and induces additional structural damping on the vibration responses [24]. However, this damping effect and the vibrational behaviour of MPPs remain to study in detail. This present work therefore proposes to model the dynamic response of microperforated plates and to investigate their structural damping capabilities. To this end, based on an MPP-porous analogy [2], a vibration approach for porous plates [21] is used to model the dynamic response of MPPs from a modal analysis. Since the diameter of the perforation and the perforation ratio have an influence on the sound absorption [18, 33–35], their effect on the damping added by the microperforation is explored.

This paper is organized as follows. Firstly, in Section 2, the present study suggests an analytical vibratory model for MPP as an extension of the works [21] and [3]. Then, in Section 3, modal analysis is performed in order to explore the MPP vibratory response along with the effect of Biot's viscous damping mechanism in the perforations. The effect of the added damping introduced by viscous friction in the perforations is determined on the eigenmodes. The validity of the approach is discussed by comparing the results of the damping factors obtained for a plate with and without microperforations. Section 4 provides a parametric study to characterize this added damping and to maximize it, in particular in the vicinity of the first vibration modes. Finally, in Section 5 an experimental study is undertaken in order to validate the proposed model and the possibility of using microperforations to improve the damping of the structure.

2. From porous plate to microperforated plates: governing equations

2.1. A microperforated plate seen as an equivalent porous plate

It is proposed to apply to the microperforated plates the models used to characterize the dynamics of a thin, finite porous plate loaded with fluid represented in Figure 1. By assumption, since the thickness of the plate is small compared to other dimensions, only bending is considered. Based on Biot's theory [5, 6], the equations of the structural dynamics of porous plates [21, 38] were established. All Johnson-Champoux-Allard (JCA) macroscopic parameters (porosity ϕ, tortuosity α_∞, airflow resistivity σ and characteristic lengths Λ and Λ') were used in these models. An approach establishing a vibration model for a finite size porous plate is proposed [21]. This model considers a finite plate of dimension $L_x \times L_y \times h$, oriented in the xy plan represented in Figure 1, excited by an external load $f_{\text{ext}}(x, y, t)$. This external load representing a force per unit length is oriented along the normal to the plate (in this case $-z$). This model defines the fluid-solid relative displacement $w(x,y,t)$ as well as that of the plate $w_\mathrm{s}(x,y,t)$ and takes the form of the two coupled equations. This system of equation describes the dynamic response of a finite porous plate saturated by a fluid in its pores and is written

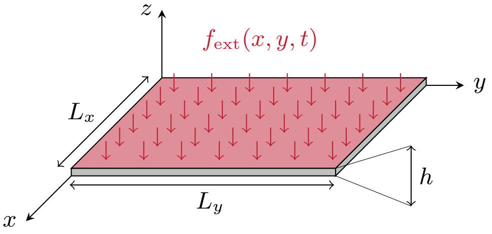

Figure 1: System of coordinates in the plate with $f_\mathrm{ext}(x,y,t)$ the external mechanical force.

$$\left(D+\frac{\alpha^2 M_\mathrm{f} h^3}{12}\right)\nabla^4 w_\mathrm{s}(x,y,t)+h(\rho\ddot{w}_\mathrm{s}(x,y,t)+\rho_\mathrm{f}\ddot{w}(x,y,t)) = f_\mathrm{ext}(x,y,t), \tag{1a}$$

$$\alpha M_\mathrm{f}\nabla^2 w_\mathrm{s}(x,y,t)-\rho_\mathrm{f}\ddot{w}_\mathrm{s}(x,y,t)-m(j\omega)\ddot{w}(x,y,t)=0, \tag{1b}$$

where $\nabla^4(\cdot)=\nabla^2(\cdot)^2$ and $\nabla^2(\cdot)=\frac{\partial^2(\cdot)}{\partial x^2}+\frac{\partial^2(\cdot)}{\partial y^2}$ and $w(x,y,t)=\phi(w_\mathrm{f}(x,y,t)-w_\mathrm{s}(x,y,t))$ with $w_\mathrm{f}(x,y,t)$ is the fluid displacements. In Equation (1), the term

$$D=\frac{Eh^3}{12(1-\nu_0^2)} \tag{2}$$

is the bending stiffness of the non-porous plate, a function of: Young's modulus[1]. E, thickness h and Poisson's coefficient ν_0. The density of the fluid-solid mixture is noted ρ. The parameter α is unitless and characterizes the elastic coupling between the equivalent fluid and the solid while the coefficient M_f is the elastic modulus of the equivalent fluid, both defined by Biot [7]. In the particular case of lightweight fluid, the two previous elastic coefficients are expressed as a function of the perforation ratio and fluid bulk modulus K_f such that [21]

$$M_\mathrm{f}\approx\frac{K_\mathrm{f}}{\phi}\quad\text{and}\quad\alpha\approx\phi. \tag{3}$$

Equation (1a) corresponds to the elastic response of the equivalent plate and Equation (1b), to the relative motion between the fluid and the solid. The viscosity of the fluid causes forces to emerge at the fluid-solid interface on both the fluid and the solid. The viscous force per unit volume is defined as a function of ω the angular frequency [6]

$$f_\mathrm{v}(x,y,t)=\sigma\phi G(j\omega)\dot{w}(x,y,t) \tag{4}$$

where the function $G(j\omega)$ is the high-frequency viscosity correction defined for the forced response[2]

$$G(j\omega)=\sqrt{1+\frac{4\alpha_\infty^2\mu_\mathrm{f}\rho_\mathrm{f}j\omega}{\sigma^2\Lambda\phi^2}}. \tag{5}$$

By considering a harmonic displacement of the $w(x,y,t)=\hat{w}(x,y)\exp(j\omega t)$ and writing $\dot{w}(x,y,t)=\frac{\ddot{w}(x,y,t)}{j\omega}$, Equation (4) becomes

$$f_\mathrm{v}(x,y,t)=\sigma\phi G(j\omega)\frac{\ddot{w}(x,y,t)}{j\omega}. \tag{6}$$

This dissipative effect is directly proportional to the viscous force generated by friction in the boundary layers in the perforations and is considered in Equation (1b) in the form of the complex coefficient

$$m(j\omega)=\frac{1}{\phi}\left(\rho_\mathrm{f}\alpha_\infty+\frac{\sigma\phi G(j\omega)}{j\omega}\right), \tag{7}$$

---

[1] It is possible to use a complex Young's modulus to achieve structural damping defined from the isotropic structural loss factor η_s. The latter is considered after the space discretization of the equations performed in Section 3.1.

[2] Equation (4) and Equation (5) could be generalized in order to carry out an analysis of free vibrations using a complex coefficient λ which considers the damping by not neglecting the real part. In the case where low damping involved, the approximation $\lambda\approx\Im\lambda\approx j\omega$ is valid.

where the second right hand-side term is the dissipation coefficient arising in $f_{\mathrm{v}}(x,y,t)$. In the low frequency limit, $G(j\omega)$ in Equation (5) can be approximated by its asymptotic limit: $\lim_{\omega\to 0} G(j\omega) = 1$. By inserting Equation (7) into Equation (1b) and using this low frequency assumption, it is possible to decompose the mass parameter in two terms: an equivalent mass term multiplying $\ddot{w}(x,y,t)$ and an equivalent damping term multiplying $\dot{w}(x,y,t)$. Equation (1) can then be recast into

$$\left(D + \frac{\alpha^2 M_{\mathrm{f}} h^3}{12}\right)\nabla^4 w_{\mathrm{s}}(x,y,t) + h(\rho \ddot{w}_{\mathrm{s}}(x,y,t) + \rho_{\mathrm{f}} \ddot{w}(x,y,t)) = f_{\mathrm{ext}}(x,y,t), \tag{8a}$$

$$\alpha M_{\mathrm{f}} \nabla^2 w_{\mathrm{s}}(x,y,t) - \left(\rho_{\mathrm{f}} \ddot{w}_{\mathrm{s}}(x,y,t) + \frac{\rho_{\mathrm{f}} \alpha_\infty}{\phi} \ddot{w}(x,y,t)\right) - \sigma \dot{w}(x,y,t) = 0. \tag{8b}$$

In the case of the study of the vibrating plate, the chosen reference frame is linked to the fluid, which results in a negative viscous force and therefore a negative relative velocity coefficient multiplying $\dot{w}(x,y,t)$ which damps the motion of the structure.

Based on the JCA model for rigid porous media, the previous formulation can be adapted to the microperforated plate. The macroscopic JCA parameters are therefore modified for the special case of MPPs [2]. In fact, for microperforated and porous plates, it is possible to decouple the viscous and thermal effects arising in the microperforations by using two complex quantities, which depend on the angular frequency ω of the response: the equivalent density $\rho_{\mathrm{e}}(\omega)$ and the equivalent fluid bulk modulus $K_{\mathrm{e}}(\omega)$. The equivalent density captures the viscous and inertial interactions between the solid frame and the fluid, while the equivalent modulus of elasticity accounts for the thermal interactions. Using this approach, all JCA parameters defined for a porous plate can also be expressed for a microperforated plate with perpendicular cylindrical pores, for which it is possible to assume that the fluid within a microperforation behaves as a Poiseuille flow involving an incompressible Newtonian fluid. The physical phenomena involved in a microperforation are recalled in Figure 2. For an MPP with perforations of circular cross-section, the static airflow resistivity indicated is [2]

$$\sigma = \frac{32\mu_{\mathrm{f}}}{\phi d^2}, \tag{9}$$

where μ_{f} is the dynamic viscosity of the fluid, ϕ, the perforation ratio, and d, the perforation diameter. For straight cylindrical pores, the viscous and the thermal characteristic lengths, respectively noted Λ and Λ', are equal to the radius of the perforation, that is $\Lambda = \Lambda' = d/2$.

Also used in the JCA's model is the tortuosity α_∞ that reflects the distortion of the fluid flow in the pore generated by a compression wave velocity. For an MPP, the perforations are straight and $\alpha_\infty = 1$. However, it is important to note that the JCA model must be modified in order to account for end correction effects caused by radiated waves and distorted flows arising in the vicinity of the perforations. The air mass contained in the perforation oscillates and radiates on both sides of the plate (Figure 2).

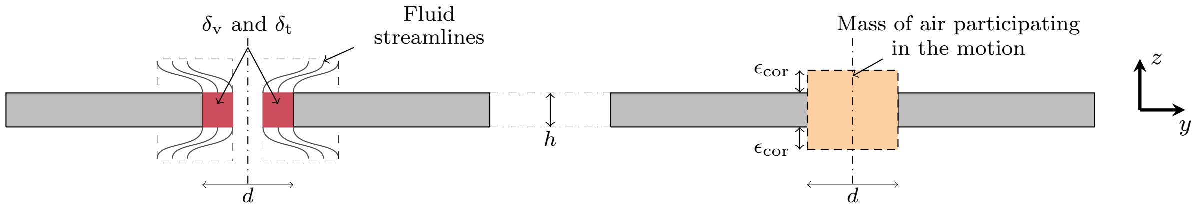

Figure 2: Physical phenomena occurring near a perforation of diameter d [2], where δ_{v} and δ_{t} are respectively the viscous and the thermal boundary layer and ϵ_{cor} is the correction length due to acoustic radiation.

The mass of air carried along during the radiation is greater than that contained in the perforation. This inertia effect increases the mass of the vibrating air and is accounted for by means of correction lengths ϵ_{cor} that must be added on both sides of the perforation so that the tortuosity thus becomes [2]

$$\alpha_\infty = 1 + \frac{2\epsilon_{\mathrm{cor}}}{h}, \tag{10}$$

where h is the plate thickness and $\epsilon_{\mathrm{cor}} = 0.24\sqrt{\pi d^2}(1 - 1.14\sqrt{\phi})$ [2]. Equation (10) is valid for a perforation ratio $\phi < 16\,\%$ and assuming that $k_0 h \ll 1$ with the wave number $k_0 = \omega/c_0$ and c_0 the wave velocity in the fluid. This factor ϵ_{cor} considers the fluid radiation inside the perforations.

In the present work, by assuming cylindrical straight perforations and using the JCA parameters for MPP, it is possible to establish a vibration model for the MPP based on Equation (8). For this purpose, all standard boundary conditions can be considered in Equation (8) assuming that the MPP is a homogeneous effective medium. In this paper, the numerical study is performed for a plate considered to be simply supported on each of its edges while the experimental study is carried out clamped-free boundary condition. For a thin plate of dimensions $L_x \times L_y \times h$, the simply-supported boundary conditions for the solid displacement, are

$$w_{\mathrm{s}}(x=0,y,t) = w_{\mathrm{s}}(x=L_x,y,t) = 0, \qquad M_x(x=0,y,t) = M_x(x=L_x,y,t) = 0, \tag{11a}$$

$$w_{\mathrm{s}}(x,y=0,t) = w_{\mathrm{s}}(x,y=L_y,t) = 0, \qquad M_y(x,y=0,t) = M_y(x,y=L_y,t) = 0, \tag{11b}$$

where M_x and M_y are the bending moments in the x and y directions, respectively.

2.2. Non-dimensional analysis of the equations of motion

The first step to simplify the analysis is to search for the dimensionless groups that control the system of equations. Every solution of an equation can be expressed as a linear relation between these dimensionless groups [11, 28]. The dimensionless system can be written as a function of $p-3$ scaled parameters, where p is the number of independent parameters, with $p=9$ in Equation (1). This can be achieved by nondimensionalizing the governing Equation (1) through classical methods [14].

Setting the external load equal to zero, the dimensionless version of Equation (1) can be expressed as a function of the $p-3=6$ dimensionless parameters: $E' = E/(12(1-\nu^2)\alpha M_{\mathrm{f}})$, $\rho' = \rho/\rho_{\mathrm{f}}$, $m' = m/\rho_{\mathrm{f}}$, $u_{\mathrm{s}} = w_{\mathrm{s}}/h$, $U = w/h$ and $\tau = t \times (\alpha M_{\mathrm{f}}/(\rho_{\mathrm{f}} h))$. The time derivative is taken with respect to the dimensionless time τ. The spatial derivatives induced by ∇^4 and ∇^2 must respect the directions x and y which are adimensionalized by the thickness h of the plate. As a result, the autonomous version of Equation (1) takes the new form

$$E'\nabla^4 u_{\mathrm{s}} + \rho' \ddot{u}_{\mathrm{s}} + \ddot{U} = 0, \tag{12a}$$

$$\nabla^2 u_{\mathrm{s}} - \ddot{u}_{\mathrm{s}} - m'\ddot{U} = 0. \tag{12b}$$

As explained in the next section, this will be used to approximate the natural frequencies and the damping factors of the microperforated plate.

2.3. Approximate natural frequencies and damping factors of microperforated plates

Leclaire *et al.* [21] derived approximate natural frequencies of a porous plate. This formulation is valid if $E \gg M_{\mathrm{f}}$, as generally accepted for rigid porous materials and for microperforated plates vibrating in surrounding air, as numerically confirmed.

In order to obtain approximate resonance frequencies and damping factors, similar assumptions are considered for MPP in the present section. From the dimensional analysis in Section 2.2, Equation (12b) is written $m'\ddot{U} = \nabla^2 u_{\mathrm{s}} - \ddot{u}_{\mathrm{s}}$ and Equation (12) can then be combined into the equation

$$E'\nabla^4 u_{\mathrm{s}} + \ddot{u}_{\mathrm{s}}\left(\rho' - \frac{1}{m'}\right) + \frac{\nabla^2 u_{\mathrm{s}}}{m'} = 0 \tag{13}$$

which only involves the dimensionless plate deflection u_{s}. Note that in the case of an MPP saturated by a low-density fluid, the term $\rho' - \frac{1}{m'}$ is approximated by ρ'. Equation (13) simplifies to

$$E'\nabla^4 u_{\mathrm{s}} + \rho' \ddot{u}_{\mathrm{s}} + \frac{\nabla^2 u_{\mathrm{s}}}{m'} = 0 \tag{14}$$

and this assumption is numerically validated. A similar expression involving the plate deflection w_{s} can be derived using the dimensional parameters of Equation (1), that is

$$D\nabla^4 w_{\mathrm{s}} + h\left(\rho \ddot{w}_{\mathrm{s}} + \frac{\rho_{\mathrm{f}}\alpha M_{\mathrm{f}}\nabla^2 w_{\mathrm{s}}}{m(j\omega)}\right) = 0. \tag{15}$$

Assuming a harmonic response along with the simply-supported boundary conditions in Equation (11) allows us to separate space and time dependencies, that is $w_{\mathrm{s}}(x,y,t) = \hat{w}_{\mathrm{s}}(x,y)\exp(\lambda t)$. After space discretization, Equation (15) is an ODE with constant coefficients. It can be written as an eigenvalue problem[3]. Solutions for the eigenmode (m,n) correspond to complex eigenvalue λ_{mn}, where m and n are the indices of the modal discretization in the x and y directions. On the context of damped system, the real part of λ_{mn} is negative and accounts for the damping of the structure, while the imaginary part corresponds to the eigen angular frequency. Solutions of Equation (15) can be obtained for a particular MPP which parameters are listed in Table 1. The diameter of the perforations is set to $d = 1.4\,\mathrm{mm}$. The numerical values of the damped eigenfrequencies γ_{mn} obtained with two approximations are listed in Table 2. The relative error is less than 3 %. However, the real parts do not match. The approach in reference [21] does not allow to depreciate the system but can be used to have an accurate estimation of the natural frequencies. This is due to the fact that in this approach, the stiffness term $\alpha M_{\mathrm{f}}\nabla^2 w_{\mathrm{s}}(x,y,t)$ is neglected. In order to consider damping in the response, Equation (15) is therefore used in this study.

---

[3] Details of space discretization and resolution are given in Section 3.2.

Microperforated plate	
L_x (mm)	490
L_y (mm)	570
h (mm)	1.0
ϕ (%)	10
d (mm)	[0.1;5]

Solid and fluid parameters	
ρ_{s} ($\mathrm{kg\,m^{-3}}$)	2680
ρ_{f} ($\mathrm{kg\,m^{-3}}$)	1.213
E (GPa)	66
K_{f} (kPa)	130
ν_0	0.3
η_{s}	10^{-4}
μ_{f} ($\mathrm{kg\,m^{-1}\,s^{-1}}$)	1.84×10^{-5}

Table 1: Implemented numerical values.

	Equation (15)		**Model** [21]	
m, n	β_{mn}	γ_{mn}	β_{mn}	γ_{mn}
1,1	-0.47	113.7	0.0008	114.4
1,2	-0.40	259.5	0.0015	260.1
2,1	-0.36	311.0	0.0016	311.6
2,2	-0.28	456.2	0.0018	457.4
1,3	-0.25	502.7	0.0018	503.3
3,1	-0.20	639.6	0.0019	640.9

Table 2: Eigenvalues $\lambda_{mn} = \beta_{mn} + j\gamma_{mn}$ for the simply-supported MPP defined in Table 1.

2.4. Biot's frequency and maximum damping

The Biot frequency noted f_{Biot} is a characteristic frequency defined by Biot [5] as

$$f_{\mathrm{Biot}} = \frac{\sigma\phi}{2\pi\rho_{\mathrm{f}}}. \tag{16}$$

This characteristic frequency separates two regimes: for $f < f_{\mathrm{Biot}}$, the inertial effect dominates while for $f > f_{\mathrm{Biot}}$ the viscous dissipation dominates. The Biot characteristic frequency is related to the thicknesses of the viscous boundary layers δ_{v}. In the particular case of cylinder pores with circular cross-section, f_{Biot} is defined when $\delta_{\mathrm{v}} = d/4$.

In the context of porous plates, it has been shown that there is a characteristic frequency equal to $f_{\mathrm{Biot}}/\alpha_\infty$ for which the viscous frictional damping of a porous plate is maximum [21]. Making this frequency coincide with the main resonance of a plate maximizes the damping of the system. It is shown in the following that similar results are observable for MPPs.

In fact, in the case of a microperforated plate, the Biot frequency can be written as a function of only one parameter that can be ϕ or d which are dependent parameters satisfying

$$\phi = \frac{N_{\mathrm{perf}}\pi d^2}{4L_xL_y} \tag{17}$$

where N_{perf} is the number of perforations in the MPP. In this document, we have chosen to consider f_{Biot} as ϕ-independent. By injecting Equation (9) in Equation (16), the Biot frequency is therefore written for an MPP only as a function of d. The characteristic frequency $f_{\mathrm{c}} = f_{\mathrm{Biot}}/\alpha_\infty$, for which the added damping is maximum, is written as follows

$$f_{\mathrm{c}} = \frac{32\mu_{\mathrm{f}}}{2\pi\alpha_\infty\rho_{\mathrm{f}}d^2}. \tag{18}$$

The corresponding angular frequency is written $\omega_{\mathrm{c}} = 2\pi f_{\mathrm{c}}$. This frequency is characteristic of viscous friction between the fluid and the solid.

3. Vibration analysis of a finite size microperforated plate

3.1. Space semi-discretization

In the framework of linear elasticity, displacements are considered small and normal to the plate surface at rest. In Equation (8), the time dependence and space dependence in $w_{\mathrm{s}}(x, y, t)$, $f_{\mathrm{ext}}(x, y, t)$ or $w(x, y, t)$ are separable and the motion can be considered as a linear combination of natural motions. Thus, Equation (8) represents a set of an infinite number of simultaneous differential equations. In the particular case where exponential type solutions are targeted, Equation (8) and the associated boundary conditions collectively constitute a bi-harmonic eigenvalue problem. Solving this problem gives access to the eigenvalues λ_{mn}

and to the modal basis functions $\Psi_{mn}(x,y)$. The deflection of the plate is then assumed to be in the following form

$$w_{\mathrm{s}}(x,y,t)=\sum_{m=1}^{\infty}\sum_{n=1}^{\infty}w_{mn}^{\mathrm{s}}(t)\Psi_{mn}(x,y) \tag{19}$$

where $w_{mn}^{\mathrm{s}}(t)$ represent the generalized coordinates of eigenmodes (m,n) that are unknown functions of t. Similar expressions are chosen for the relative fluid-structure modal displacement with the t-function $w_{mn}(t)$. Indeed, for a microperforated structure, it is assumed that the same boundary conditions and basis expansions are used for the displacement fields of both the plate and the fluid [38]. In the case of the present study, the fluid within the perforations is considered as an effective fluid taking the shape of an equivalent fluid plate and the perforated solid is considered as an effective solid taking the shape of an equivalent solid plate. For a mechanical excitation, the motion of the equivalent fluid plate is related to that of the equivalent solid plate and therefore it is reasonable to consider that the boundary conditions are the same for both plates.

The basis functions $\Psi_{mn}(x,y)$ are chosen as a linear combination of hyperbolic and trigonometric functions. For a rectangular plate, $\Psi_{mn}(x,y)=\phi_m(x)\phi_n(y)$ where

$$\phi_k(\xi)=A_k\cosh\Omega_k\xi+B_k\cos\Omega_k\xi+C_k\sinh\Omega_k\xi+D_k\sin\Omega_k\xi. \tag{20}$$

The basic functions for particular boundary conditions are presented in Appendix A. In order to simplify the notations, we decided to reorganize the $\Psi_{mn}(x,y)$ into a single index expression $\Psi_i(x,y)$. Equation (19) can be therefore rewritten for a finite number of modes such that

$$w_{\mathrm{s}}(x,y,t)=\sum_{i=1}^{N}w_i^{\mathrm{s}}(t)\Psi_i(x,y)\quad\text{with}\quad i=1,2,\cdots,N \tag{21}$$

where N is the number of degrees-of-freedom (dof) in the discretization. In this reorganization, each pair of indices $(m,n)\in\mathbb{N}\times\mathbb{N}$ is ordered lexicographically in order to correspond to a single index $i\in\mathbb{N}$. Thus $(1,1)$ is the smallest element, the next is $(1,2)$ then $(1,3),(1,4),\cdots,(1,\frac{N}{2}),\cdots,(2,1),\cdots,(3,1),\cdots,(\frac{N}{2},1),\cdots$, in the particular case where the number of dof in x and y discretization are equal to $\frac{N}{2}$. The same reorganization of indices is performed for $w(x,y,t)$ and for $f_{\mathrm{ext}}(x,y,t)$ and is used here and in the rest of this document.

The resolution of Equation (8) involves the discretization and projection of the equations onto the plate and fluid eigenmode basis. From the above modal expansion and a space semi-discretization procedure, Equation (8) can be written in a matrix form

$$\dot{\mathbf{z}}(t)+\mathbf{D}\mathbf{z}(t)=\mathbf{f}(t), \tag{22}$$

where

$$\mathbf{D}=\begin{bmatrix}\mathbf{0} & -\mathbf{Id}\\ \mathbf{M}^{-1}\mathbf{K} & \mathbf{M}^{-1}\mathbf{C}\end{bmatrix},\quad \mathbf{z}(t)=\begin{pmatrix}\mathbf{x}(t)\\ \dot{\mathbf{x}}(t)\end{pmatrix}\quad\text{and}\quad \mathbf{f}(t)=\begin{bmatrix}\mathbf{0}\\ \mathbf{M}^{-1}\mathbf{q}(t)\end{bmatrix} \tag{23}$$

with

$$\mathbf{x}(t)=\begin{pmatrix}\mathbf{w}_{\mathrm{s}}(t)\\ \mathbf{w}(t)\end{pmatrix};\quad \mathbf{M}=\begin{bmatrix}\mathbf{M}_{\mathrm{s}_1} & \mathbf{M}_1\\ \mathbf{M}_{\mathrm{s}_2} & \mathbf{M}_2\end{bmatrix};\quad \mathbf{C}=\begin{bmatrix}\mathbf{0} & \mathbf{0}\\ \mathbf{0} & \mathbf{C}_2\end{bmatrix};\quad \mathbf{K}=\begin{bmatrix}\mathbf{K}_1 & \mathbf{0}\\ \mathbf{K}_2 & \mathbf{0}\end{bmatrix}, \tag{24}$$

and $\mathbf{q}(t)$ is the vector that stores external excitation terms. Boldface notations represent vectors or matrices. The vector $\mathbf{x}(t)$ stores both solid and relative fluid-solid displacements, respectively $\mathbf{w}_{\mathrm{s}}(t)$ and $\mathbf{w}(t)$, and is defined relatively to an equilibrium position when the structure is at rest. The vector $\mathbf{w}_{\mathrm{s}}(t)$ contains the inputs $w_i^{\mathrm{s}}(t)$ while the vector $\mathbf{w}(t)$ stores the entries $w_i(t)$, both defined via the space-time decomposition presented in Equation (21). The matrices $\mathbf{M}_{\mathrm{s}_k}$, $\mathbf{M}_k$, $\mathbf{K}_k$ with $k=1,2$ and $\mathbf{C}_2$ can be obtained via a discretization by projection on the eigenmodes of the plate

$$\begin{aligned}
\mathbf{M}_{\mathrm{s}_1}&=h\rho\iint_S\mathbf{\Psi}(x,y)\mathbf{\Psi}^{\mathrm{T}}(x,y)\,\mathrm{d}x\,\mathrm{d}y, & \mathbf{M}_{\mathrm{s}_2}&=-\rho_{\mathrm{f}}\iint_S\mathbf{\Psi}(x,y)\mathbf{\Psi}^{\mathrm{T}}(x,y)\,\mathrm{d}x\,\mathrm{d}y,\\
\mathbf{M}_1&=h\rho_{\mathrm{f}}\iint_S\mathbf{\Psi}(x,y)\mathbf{\Psi}^{\mathrm{T}}(x,y)\,\mathrm{d}x\,\mathrm{d}y, & \mathbf{M}_2&=-\frac{\rho_{\mathrm{f}}\alpha_\infty}{\phi}\iint_S\mathbf{\Psi}(x,y)\mathbf{\Psi}^{\mathrm{T}}(x,y)\,\mathrm{d}x\,\mathrm{d}y,\\
\mathbf{C}_2&=-\sigma\iint_S\mathbf{\Psi}(x,y)\mathbf{\Psi}^{\mathrm{T}}(x,y)\,\mathrm{d}x\,\mathrm{d}y, & \mathbf{K}_2&=\alpha M_{\mathrm{f}}\iint_S\Delta\mathbf{\Psi}(x,y)\mathbf{\Psi}^{\mathrm{T}}(x,y)\,\mathrm{d}x\,\mathrm{d}y,\\
\mathbf{K}_1&=\left(D+\frac{\alpha^2M_{\mathrm{f}}h^3}{12}\right)\iint_S\Delta^2\mathbf{\Psi}(x,y)\mathbf{\Psi}^{\mathrm{T}}(x,y)\,\mathrm{d}x\,\mathrm{d}y
\end{aligned} \tag{25}$$

where S is the plate surface i.e. $\iint_S = \int_0^{L_x}\int_0^{L_y}$. In Equation (25), $\mathbf{\Psi}(x,y)$ is the column vector that stores the entries $\Psi_i(x,y)$ and $\Delta = \nabla^2$ is the Laplacian operator, applied to each term of $\mathbf{\Psi}(x,y)$. Also, the damping matrix $\mathbf{C}_2$ is a function of σ and thus d. It accounts for friction in the perforations and can be considered as a viscous damping. The structural damping of the perforated panel can be considered by taking a complex bending stiffness defined from the isotropic structural loss factor η_s of the material constituting the MPP. In this case, $\mathbf{K}$ has complex entries: the real parts correspond to rigidity terms and the imaginary part, to damping terms. The low depreciation involved making it possible to obtain $\mathbf{D}$ in real form. The damping matrix $\mathbf{C}$ and the stiffness matrix $\mathbf{K}$ are rewritten such that

$$\mathbf{C} = \begin{bmatrix} \mathbf{C}_1 & \mathbf{0} \\ \mathbf{0} & \mathbf{C}_2 \end{bmatrix} \quad \text{and} \quad \mathbf{K} = \begin{bmatrix} \Re\mathbf{K}_1 & \mathbf{0} \\ \mathbf{K}_2 & \mathbf{0} \end{bmatrix}. \tag{26}$$

where each coefficient in $\mathbf{C}_1$ is its equivalent coefficient in $\Im\mathbf{K}_1$ divided by the corresponding ω_i, the ith frequency obtained for an undamped system. The matrix $\mathbf{D}$, presented in Equation (23) is therefore λ-independent.

3.2. Modal analysis

In order to study the free vibration modal motions of the microperforated structure, the external force in Equation (8) is set to $\mathbf{f}(t) = \mathbf{0}$ and Equation (22) is reduced to $\dot{\mathbf{z}}(t) + \mathbf{D}\mathbf{z}(t) = \mathbf{0}$. Modal analysis is performed in order to determine the natural modes of vibration and the associated frequencies and damping coefficients. Equation (22) represents a homogeneous set of Ordinary differential equation (ODE) with constant coefficients. Its solution can be written in exponential form as

$$\mathbf{z}(t) = \hat{\mathbf{z}}\exp(\lambda t), \tag{27}$$

where λ and $\hat{\mathbf{z}}$ respectively are a scalar and a vector. By inserting Equation (27) into Equation (22) and dividing all term by the non-vanishing $\exp(\lambda t)$, the eigenvalue problem

$$\mathbf{D}\hat{\mathbf{z}} = \lambda\hat{\mathbf{z}} \tag{28}$$

is obtained. The matrix $\mathbf{D}$ is real and the solutions of Equation (28) provides $4N$ eigensolutions. Due to the structure of $\mathbf{K}$, the solutions for the structural modes and those for the relative fluid-structure modes are decoupled: $2N$ solutions correspond to the structural modes and $2N$ to the relative fluid-structure modes.

Since the boundary conditions are simply-supported, the modes are orthogonal, $\mathbf{D}$ has a block diagonal structure

$$\mathbf{D} = \begin{bmatrix} \mathbf{D}_1 & & \\ & \ddots & \\ & & \mathbf{D}_N \end{bmatrix}, \tag{29}$$

where $\mathbf{D}_i$ is a 4×4 block defined for mode i. The resulting characteristic equation $\det(\mathbf{D}_i - \lambda\mathbf{I}) = 0$ translates into

$$\lambda^4 - d_{44_i}\lambda^3 + d_{31_i}\lambda^2 - (d_{31_i}d_{44_i} - d_{34_i}d_{41_i})\lambda = 0 \tag{30}$$

where d_{pq_i} is entry pq in $\mathbf{D}_i$. The chosen formulation of the model presented in Equation (8) which contains no w terms. This results in a rigid body motion of the fluid and thus a zero eigenvalue, which corresponds to the trivial solution $\lambda = 0$ in Equation (30). The other three roots of Equation (30) are positive real or complex conjugates. Eigenvalues corresponding to structure displacement are complex conjugates $\lambda_i = \beta_i \pm j\gamma_i$ where the imaginary part $\Im\lambda_i = \gamma_i = \omega_i\sqrt{1-\zeta_i^2}$ is the natural frequency of the mode i for the damped system and the real part $\Re\lambda_i = \beta_i = -\zeta_i\omega_i$, the damping term involved in the exponential decrease of the mode, expressions in which ω_i is the natural frequency of the undamped mode i and ζ_i, the corresponding modal damping ratio. Motions in the underdamped modes consist of decaying oscillations, which can be described as a system of two coupled first-order differential equations in time. Details of modal resolution for a one-dof dissipative system are presented in Appendix B. Four eigenmodes $\hat{\mathbf{z}}_k$, with $k \in [1;4]$, corresponding to eigenvalues, λ_k are defined where $\hat{\mathbf{z}}_1$ and $\hat{\mathbf{z}}_2$ are complex conjugate while $\hat{\mathbf{z}}_3$ and $\hat{\mathbf{z}}_4$ are purely real. Also, the eigenvalue corresponding to $\hat{\mathbf{z}}_3$ is 0.

It is possible to perform a projection on the modal basis $\mathbf{z}_i(t) = \mathbf{P}_i\mathbf{u}_i(t)$ where each 4×4 $\mathbf{P}_i$ matrix is organized as follows:

$$\mathbf{P}_i = \begin{bmatrix} \Re\hat{\mathbf{z}}_1 & \Im\hat{\mathbf{z}}_1 & \hat{\mathbf{z}}_3 & \hat{\mathbf{z}}_4 \end{bmatrix}_i. \tag{31}$$

Contrary to the modal forms $\Psi_i(x,y)$, which allow the discretization in the space of the equations, the $\mathbf{P}_i$ modes correspond to the diagonalization modes, resulting from the projections of the discretized equations on the modal basis. After projection in the modal basis, Equation (22) takes the block matrix form

$$\dot{\mathbf{u}}_i(t) = \mathbf{L}_i \mathbf{u}_i(t), \quad \text{with} \quad \mathbf{L}_i = \mathbf{P}_i^{-1}\mathbf{D}_i\mathbf{P}_i = \begin{bmatrix} \beta_1 & \gamma_1 & 0 & 0 \\ -\gamma_1 & \beta_1 & 0 & 0 \\ 0 & 0 & 0 & 0 \\ 0 & 0 & 0 & \beta_4 \end{bmatrix}_i . \tag{32}$$

For block i, the equations are (the index i and the time dependency are dropped for readability purposes)

$$\dot{u}_1 = \beta_1 u_1 + \gamma_1 u_2, \tag{33a}$$
$$\dot{u}_2 = -\gamma_1 u_1 + \beta_1 u_2, \tag{33b}$$
$$\dot{u}_3 = 0, \tag{33c}$$
$$\dot{u}_4 = \beta_4 u_4. \tag{33d}$$

The mapping back to the physical basis is possible by multiplying the vector $\mathbf{u}_i(t)$, resulting from the resolution of Equation (33) by the change of basis matrix $\mathbf{P}_i$.

3.3. Forced response analysis

The modal analysis is sufficient for the mechanical analysis of the MPP and allows for simple parametric analyses. However, microperforated plates can also be excited by a mechanical force acting at a particular location on the structure, for example. In order to simulate real experimental conditions, it is important to study the forced response to an external mechanical excitation. For this purpose, a harmonic pointwise external excitation of amplitude F_{ext} is applied at (x_0, y_0) with the angular frequency ω. The punctual external load is therefore written for the ith mode such that $f_{\text{ext}_i}(x_0, y_0, t) = F_{\text{ext}}\Psi_i(x_0, y_0)\exp(j\omega t)$. The same approach presented in Section 3.2 is performed for the forced response. In this aim, after the proper projection on the considered basis of shape function, Equation (22) become

$$\dot{\mathbf{u}}_i(t) = \mathbf{L}_i \mathbf{u}_i(t) + \mathbf{P}_i^{-1}\mathbf{f}_i(t), \tag{34}$$

where $\mathbf{f}_i(t)$ is the restriction of $\mathbf{f}(t)$ to block i. Equation (32) therefore reads (again for block i)

$$\dot{u}_1 = \beta_1 u_1 + \gamma_1 u_2 + f_1, \tag{35a}$$
$$\dot{u}_2 = -\gamma_1 u_1 + \beta_1 u_2 + f_2, \tag{35b}$$
$$\dot{u}_3 = f_3, \tag{35c}$$
$$\dot{u}_4 = \beta_4 u_4 + f_4. \tag{35d}$$

In Equation (35), the f_{k_i} terms correspond to the kth term in each i block of the matrix $\mathbf{f}(t)$ defined in Equation (23). The modal participation of the forced response is obtained by solving Equation (35) for the steady state in the form

$$\mathbf{u}_i(t) = \mathbf{a}_i(\omega)\cos\omega t + \mathbf{b}_i(\omega)\sin\omega t \tag{36}$$

where $\mathbf{a}_i(\omega)$ and $\mathbf{b}_i(\omega)$ represent the modal participation in the forced response, with modulus $\mathbf{c}_i(\omega) = \sqrt{\mathbf{a}_i(\omega)^2 + \mathbf{b}_i(\omega)^2}$.

4. Sensitivity analysis

4.1. Sensitivity of the MPP vibratory forced response to fluid load

In this section, in addition to the fluid in the perforations, the external fluid is taken into account. The MPP is considered to be in a semi-infinite fluid medium. Indeed, when a structure vibrates in a fluid, it radiates acoustic waves, and it is required to account for the fluid-structure interaction [3]. The fluid loading is introduced in Equation (1) by adding a coupling term, depending on $w_k^{\text{s}}(t)$. To capture the effect of the fluid loading, it is proposed to add an acoustic source, expressed as

$$q_i(x,y,t) = -j\omega \sum_{k=1}^{\infty} Z_{ik}(1-\phi)w_k^{\text{s}}(t)\Psi_k(x,y) \tag{37}$$

where Z_{ik} is the ik element in the acoustic radiation impedance tensor. The reorganization of indices presented in Equation (21) is used here. The effect of radiation at the orifice of the perforation is already active via the correction term ϵ_{cor} [2]. Only the displacement of the solid multiplied by the proportion of the surface of the solid is considered, via the term $(1-\phi)w_k^{\mathrm{s}}(t)$. The cross-coupling coefficients in the radiation impedance tensor are given by [31]

$$Z_{ik} = j\omega\rho_{\mathrm{f}} \int_S \int_{S'} \Upsilon_{ik}(x,y,x',y')\,\mathrm{d}S'\,\mathrm{d}S \tag{38}$$

where $\Upsilon_{ik}(x,y,x',y') = \Psi_i(x,y)G_{\mathrm{r}}(x,y,x',y')\Psi_k(x',y')$. The Green function $G_{\mathrm{r}}(x,y,x',y')$, associated with the contribution of a surface element S', is defined by

$$G_{\mathrm{r}}(x,y,x',y') = \frac{\exp(jrk_0)}{2\pi r}, \tag{39}$$

where r is given by $r = \sqrt{(x-x')^2+(y-y')^2}$. The factor $1/2\pi$ in Equation (39) is used in the case presented here for a baffle plate. For a non-baffle plate, this factor must be replaced by $1/4\pi$. When the receiving and transmitting elements are the same, the distance r becomes zero and the Green function (39) becomes infinite. In order to ensure the convergence of the integral, the solution proposed in this work to deal with this singularity is to use a limit formulation when r is close to zero. In order to compute Equation (22), the surface is discretized into small segments. The integral formulation of the radiation impedance is therefore expressed as a discrete problem, with n_{b} elements in the discretization. A quadruple Riemann sum is performed in order to obtain a numerical approximation of Equation (38).

The acoustic load, represented by the radiation impedance, has two effects. First, it modifies the damping of the plate-air system represented by $\Re Z_{ik}$. Second, it adds a reactive effect to the plate-air system by the addition of a mass represented by $\Im Z_{ik}$. For a low-density fluid (e.g. air), the cross-coupling terms can be neglected, so that $Z_{ik} = 0$ if $i \neq k$. The radiation impedance matrix is thus a diagonal matrix.

Finally, Z_{ik} is inserted in Equation (8) through the load

$$q_{\mathrm{rad}}(x,y,t) = \sum_{i=1}^{\infty} q_i(x,y,t), \tag{40}$$

where q_i is defined in Equation (37). The fluid-loaded system can thus be modelled, for an MPP immersed in a low-density fluid, as

$$\Big(D + \frac{\alpha^2 M_{\mathrm{f}} h^3}{12}\Big)\nabla^4 w_{\mathrm{s}} + h(\rho\ddot{w}_{\mathrm{s}} + \rho_{\mathrm{f}}\ddot{w}) = f_{\mathrm{ext}} + q_{\mathrm{rad}}, \tag{41a}$$

$$\alpha M_{\mathrm{f}} h \nabla^2 w_{\mathrm{s}} - h\Big(\rho_{\mathrm{f}}\ddot{w}_{\mathrm{s}} + \frac{\rho_{\mathrm{f}}\alpha_\infty}{\phi}\ddot{w}\Big) - h\sigma\dot{w} = q_{\mathrm{rad}}. \tag{41b}$$

After space discretization and projection onto plate mode shape, Equation (41) is solved by using the approach presented in Section 3.2. For a microperforated plate loaded with low-density fluid, the modal diagram is negligibly modified by the parietal pressure induced by the fluid on the plate. A comparison of the eigenfrequency γ_i and corresponding modal damping ratio ζ_i between a simply-supported MPP saturated by air and an MPP *in vacuo* is undertaken in Table 3. It appears that in the case of an air-saturated plate, the fluid loading has a negligible effect on the natural frequencies and damping rates.

	1. *in vacuo*		2. in air	
i	γ_i	ζ_i	γ_i	ζ_i
1	113.97	4.071×10^{-3}	113.95	4.079×10^{-3}
2	259.39	1.536×10^{-3}	259.37	1.537×10^{-3}
3	310.82	1.148×10^{-3}	310.80	1.149×10^{-3}
4	456.51	0.584×10^{-3}	456.50	0.585×10^{-3}

Table 3: Modal characteristic of mode i for the microperforated plate defined in Table 1 with $d = 1.4\,\mathrm{mm}$ and η_{s} set to zero. Eigenfrequency γ_i in $\mathrm{rad\,s^{-1}}$ and the corresponding modal damping ratio ζ_i.

4.2. Free vibratory response sensitivity to perforation ratio

Two parameters can have a significant influence on the MPP vibratory response: ϕ and d. The other parameters (σ, α_∞, Λ and Λ') are dependent on ϕ and d. For an MPP, the higher ϕ, the less rigid is the structure. In order to maintain the mechanical properties of the material (E and ρ_{s}) for an MPP close to those of the non-perforated structure, the perforation ratio must remain low, typically below 16 % in our study. Moreover, Biot's damping stems from viscous friction coupling with fluid-structure interaction. Then, since losses occur in the perforations, the greater the number of perforations of a

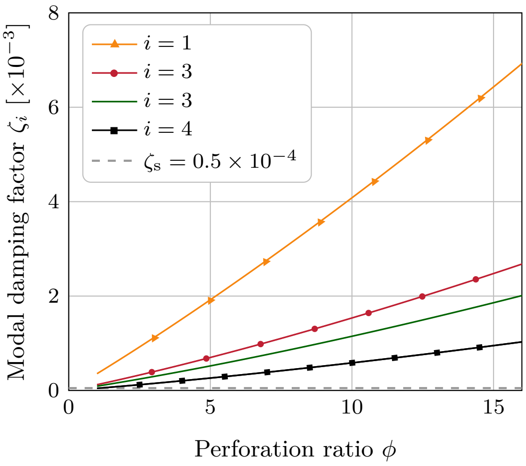

Figure 3: Modal damping factor sensitivity to ϕ for a simply-supported MPP (see Table 1) with $d = 1.4\,\text{mm}$. The isotropic structural loss factor $\eta_s = 2\zeta_s$ is assumed constant for each mode i.

given d, the greater the damping. For the MPP described in Table 1, the influence of ϕ for a given perforation diameter on the modal damping ratio of the first four mode shapes are presented in Figure 3. The constant perforation diameter is set to $d = 1.4\,\text{mm}$. The comparison between the added damping and the structural damping is also provided in Figure 3. The structural damping for the ith mode $\eta_s = 2\zeta_s$ is assumed to be constant and ϕ-independent. Value of η_s for an alumium plate is given in Table 1. In the present study, all microperforations have the same geometry and diameter. In this case, f_c is chosen to be expressed as a function d. The perforation ratio therefore has negligible influence on f_c but might slightly perturb the natural frequencies by changing the mass and stiffness matrices. A correction of the Young modulus [8, 39] can thus be applied on ϕ so that

$$E_{\text{eq}}(\phi) = E \frac{(1-\phi)^2}{1 + (2 - 3\nu_0)\phi}, \tag{42}$$

where E and ν_0 are respectively the Young's modulus and the Poisson's ratio of the non-perforated plate. Equation (42) is included in the analytical model. Microperforations also affect the mass matrix by defining an equivalent structure density such that $\rho = \rho_s(1-\phi) + \phi\rho_f$. In the particular case of a low-density fluid, the equivalent density ρ can be approximated by $\rho = \rho_s(1-\phi)$. Vibratory resonance occurs at lower frequencies for an MPP than for a non-perforated plate of the same size. An approximation of the natural resonance frequencies for a finite size MPP saturated by a lightweight fluid is possible from the resonant frequencies of the non-perforated plate. The resonance frequencies of an MPP can therefore be obtained using the well-known plate resonance formulae. The equivalent equation of motion for mode i considering the equivalent material properties of the MPP (i.e. ρ and $E_{\text{eq}}(\phi)$) can be written as

$$M_i(1-\phi)\ddot{w}_i^{s}(t) + K_i\Big(\frac{(1-\phi)^2}{1+(2-3\nu_0)\phi}\Big)w_i^{s}(t) = 0. \tag{43}$$

As a first approach, the corresponding natural resonance frequencies are

$$\omega_i = \delta(\phi)\sqrt{K_i/M_i} \quad \text{where} \quad \delta(\phi) = \sqrt{\frac{1-\phi}{1+(2-3\nu_0)\phi}}. \tag{44}$$

The natural frequencies of the MPP are therefore approximately $\delta(\phi)$ off from the natural frequencies of a non-perforated plate. Natural angular frequencies for an MPP considering the Young modulus correction are given in Table 4. A comparison of angular frequencies calculated from the approximate formula of Equation (44) and the full model given in Equation (8) for an MPP is presented in Table 4. Approximate values of angular frequencies for the MPP are obtained from those calculated analytically for a non-perforated plate through Equation (44). The values presented in Table 4 are obtained for $\eta_s = 0$ and γ_i corresponds to the imaginary part of the eigenvalues that considered the damping induced by the microperforations. The relative error between the approximate formula and the full model is less than 1 %. The approximate formula Equation (44) does not consider the visco-thermal damping added by the microperforations which explain the relative error between the two approaches.

4.3. Free vibratory response sensitivity to perforation diameter

In order to better understand the added damping, it is proposed to plot the modal damping ratios in terms of d. Indeed, from modal analysis, the modal damping factor is given by $\zeta_i = -\beta_i/\omega_i$. For a

	Non-perforated plate	**Microperforated plate**	
i	ω_i	ω_i (44)	γ_i (8)
1	105.5	98.0	97.7
2	246.8	223.1	222.3
3	295.6	267.3	266.4
4	433.9	392.3	391.3

Table 4: Angular frequencies in rad s^{-1} of mode i for the simply-supported MPP calculated from Equation (44) and equivalent non-perforated plate defined in Table 1 with $d = 1.4$ mm. The shift factor $\delta(0.1) = 0.9$ is calculated from Equation (44). Values obtained from approximated formula (44) are compared to those calculated from the full model (8).

microperforated plate, defined in Table 1, Figure 4 shows the modal damping as a function of d, for a given ϕ. Each curve corresponds to a mode and exhibits a maximal damping induced by the optimal perforation diameter for which the modal frequency of mode i is equal to the damping characteristic frequency. When d tends to infinity, the added damping tends to zero, irrespective of ϕ. For constant perforation ratio and a specified plate size, maximum damping is obtained for the first four mode shapes. The added damping by the microperforations thus has a clear effect on low frequencies $f < 32\mu_\mathrm{f}/(\pi d^2)$.

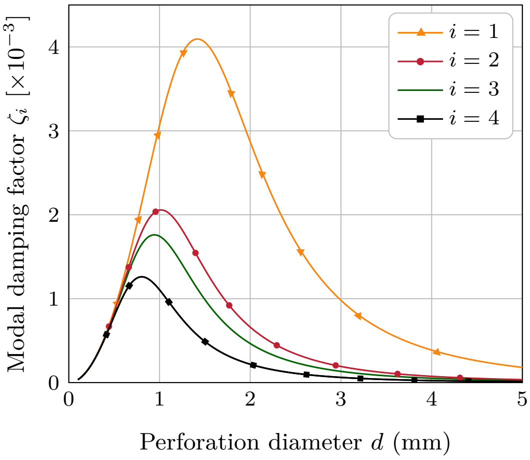

Figure 4: Modal damping sensitivity to d for a simply-supported MPP of dimensions 490 mm × 570 mm × 1 mm for $\phi = 10\,\%$.

4.4. Free vibratory response sensitivity to resonance frequencies

The viscous dissipation in materials can be included in Equation (15) by defining a complex stiffness matrix using a loss factor η_i so that Equation (15) reads

$$M_i\ddot{w}_i^\mathrm{s}(t) + K_i(1 + j\eta_i)w_i^\mathrm{s}(t) = 0 \tag{45}$$

where M_i and K_i correspond respectively to the ith element of the restriction of the mass and stiffness matrices to their diagonal terms. The approximate Equation (15) is cast into a form similar to that of an oscillating system for each mode i as

$$\left(\rho + \frac{I_i^{(2)}\rho_\mathrm{f}^2\alpha M_\mathrm{f}\phi^2\alpha_\infty}{I_i^{(3)}((\alpha_\infty\phi\rho_\mathrm{f}\omega)^2 + b_\mathrm{f}^2)}\right)\ddot{w}_i^\mathrm{s}(t) + \left(-hj\omega\frac{I_i^{(2)}\alpha M_\mathrm{f}\phi^2\rho_\mathrm{f}b_\mathrm{f}}{I_i^{(3)}((\alpha_\infty\phi\rho_\mathrm{f}\omega)^2 + b_\mathrm{f}^2)} + \frac{DI_i^{(1)}}{I_i^{(3)}}\right)w_i^\mathrm{s}(t) = 0 \tag{46}$$

where $b_\mathrm{f} = \sigma\phi^2$ is the friction coefficient defined by Biot [5]. The terms $I_i^{(k)}$ are the i contribution terms on the diagonal in the projection matrix $\mathbf{I}^{(k)}$ defined

$$\mathbf{I}^{(1)} = \iint_S \Delta^2\mathbf{\Psi}(x,y)\mathbf{\Psi}^\mathrm{T}(x,y)\,\mathrm{d}x\,\mathrm{d}y, \tag{47a}$$

$$\mathbf{I}^{(2)} = \iint_S \Delta\mathbf{\Psi}(x,y)\mathbf{\Psi}^\mathrm{T}(x,y)\,\mathrm{d}x\,\mathrm{d}y, \tag{47b}$$

$$\mathbf{I}^{(3)} = \iint_S \mathbf{\Psi}(x,y)\mathbf{\Psi}^\mathrm{T}(x,y)\,\mathrm{d}x\,\mathrm{d}y. \tag{47c}$$

By identification of Equation (46) and Equation (45), the modal loss factor is expressed as

$$\eta_i(\omega) = -\frac{h\omega I_i^{(2)}}{DI_i^{(1)}}\left(\frac{\alpha M_\mathrm{f}\phi^2\rho_\mathrm{f}b_\mathrm{f}}{(\alpha_\infty\phi\rho_\mathrm{f}\omega)^2 + b_\mathrm{f}^2}\right). \tag{48}$$

At the eigenfrequency γ_i, the loss factor is related to the modal damping factor by the following expression $\eta_i(\gamma_i) = 2\zeta_i$. From Equation (48), it is proposed to explore the influence of the resonance frequencies on η_i, as illustrated in Figure 5.

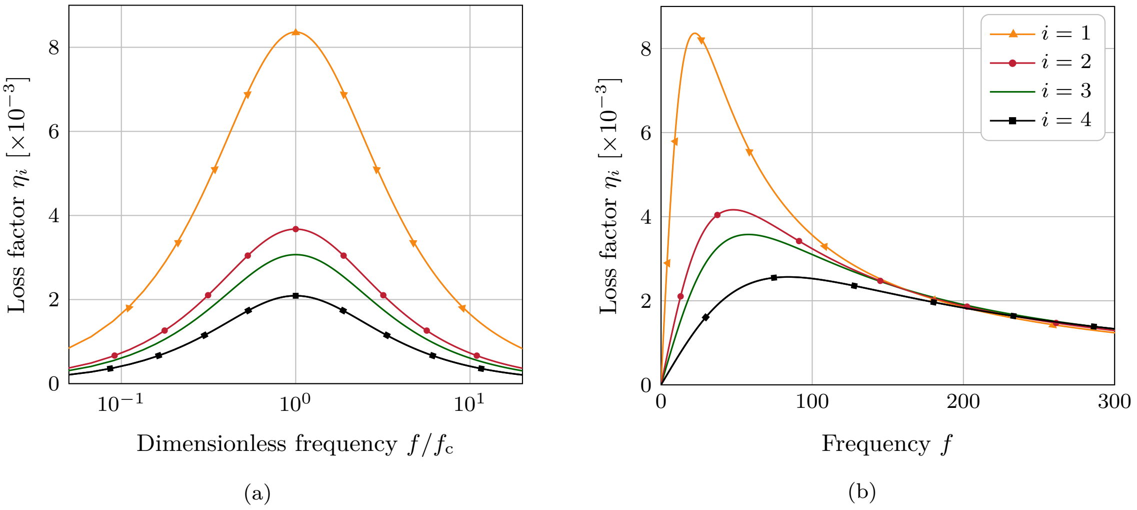

(a)

(b)

Figure 5: Loss factor given in Equation (48) for a simply-supported MPP of dimensions 490 mm × 570 mm × 1 mm (see Table 1) as function of frequency. In Figure 5(a) the diameter is fixed and f_c is a constant. The diameter is chosen to maximize the damping on f_1, we therefore have $f_1 = f_c$. In Figure 5(b) the diameter is different for each mode and is chosen to maximize the damping in each mode. We therefore have $f_i = f_c$.

Figure 5(a) shows the loss factor presented in Equation (48) as a function of dimensionless frequency for a plate with constant ϕ. The frequency is normalized with respect to f_c defined in Equation (18). The diameter of the perforations has been chosen to induce the maximum damping in the first mode. Accordingly, the characteristic frequency is identical for all modes in Figure 5(a). In Figure 5(b), the perforation diameter is not a constant and has been chosen to maximize the damping for each mode i such that

$$d_i^{\mathrm{op}} = \sqrt{\frac{32\mu_\mathrm{f}}{\omega_i \rho_\mathrm{f} \alpha_\infty}}. \tag{49}$$

The characteristic frequency which is a function d is different for each mode.

In both figures, for each mode i, η_i passes through a maximum at an optimal frequency function of d that corresponds to f_c defined in Equation (18). By inserting Equation (18) in Equation (48), a formulation of the maximum damping $\eta_i^{\max}$ is obtained, for the i mode, as

$$\eta_i^{\max} = -\frac{h\phi\alpha M_\mathrm{f} I_i^{(2)}}{2D\alpha_\infty I_i^{(1)}}. \tag{50}$$

This maximum depends on the geometry of the plate, the boundary conditions and d.

Let us now consider the asymptotic behaviours of $\eta_i(\omega)$ in Equation (48). The high frequency limit is $\lim_{\omega\to\infty} \eta_i(\omega) = 0$ for mode i. This might be explained by the fact that at high frequencies, the thermal and viscous boundary layers

$$\delta_\mathrm{v} = \sqrt{\frac{2\mu_\mathrm{f}}{\omega\rho_\mathrm{f}}} \quad \text{and} \quad \delta_\mathrm{t} = \sqrt{\frac{2\mu_\mathrm{f}}{\mathrm{Pr}\,\omega\rho_\mathrm{f}}} \tag{51}$$

respectively, where Pr is the Prantl number, become very thin and tend to the zero thickness limit since they are inversely proportional to the pulsation ω. In the high frequency limit, the fluid slides in the perforations and the damping induced in the boundary layers (thermal and viscous) becomes negligible. In the very low frequency limit, the boundary layers become very large, the fluid flow associated with the acoustic wave is totally prevented from entering the perforation and no friction in the boundary layers occurs. As a consequence, no damping mechanism by viscous friction takes place. Between these two limits, the Biot damping emerges and reaches a maximum, depending on the viscous friction losses.

It is worthy to pay attention to the frequency range over which the damping is effective. Indeed, for a given mode, the added viscous damping effect is maximal when the plate frequency coincides with f_c, but it acts on a larger bandwidth around this maximal characteristic frequency. In Figure 5(b), the Biot damping acts over a wider range of frequencies when the perforation diameter is chosen to damp higher frequency modes. This is due to the fact that, for low frequencies, the thickness of the boundary layers varies rapidly with ω. A small change in frequency will result in a larger change in the boundary layer thickness. In the high frequency limit, the boundary layer thickness can also vary with frequency, and the Biot damping will be effective over multiple modes. Accordingly, the choice of perforation diameter will certainly be a trade-off between the range over which the damping applies and its value.

4.5. Free vibratory response sensitivity to plate thickness

The plate thickness h has also a influence on the added damping. The loss factor given in Equation (48) for three MPPs with different thickness sizes is provided in Figure 6 for constant d and ϕ. In order to have the same resonance frequency of the first plate mode for the three MPPs considered, (i.e. $f_1 = 18.2\,\mathrm{Hz}$), both dimensions L_x and L_y are adjusted. The frequency is thus normalized with respect to f_1. According to Figure 6, the added damping increases as the thickness of the plate decreases for a constant resonance frequency. In order to better understand the damping sensitivity to h, an expression of the loss factor that capture the thickness effect can be developed from Equation (48). In fact, by considering only the equivalent response of the solid without the fluid contribution, the pulsation ω_i writes in terms of h

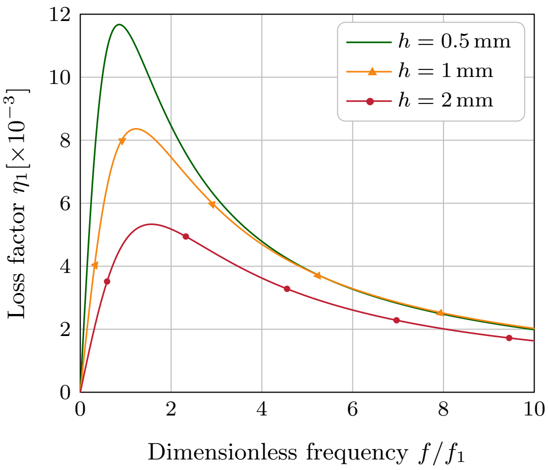

Figure 6: First mode loss factor given in Equation (48) as function of dimensionless frequency for three simply-supported MPP of dimension: (——) 346 mm × 403 mm × 0.5 mm, (—▲—) 490 mm × 570 mm × 1 mm and (—●—) 693 mm × 806 mm × 2 mm. The dimensions of the three MPPs have been chosen so that their first resonance frequency of the undamped system, f_1 is identical. The parameters of the perforations are set for the three MPPs to $d = 1.4\,\mathrm{mm}$ and $\phi = 10\,\%$.

$$\omega_i = A_i h \quad \text{where} \quad A_i = \sqrt{\frac{EI_i^{(1)}}{12\rho(1-\nu_0^2)I_i^{(3)}}}. \tag{52}$$

A formulation can be derived by inserting Equation (52) into Equation (48). The loss factor is then written in terms of h

$$\eta_i(h) = \frac{B_i^{(1)}}{B_i^{(2)}h^3 + B^{(3)}h} \quad \text{where} \quad B_i^{(1)} = \frac{-I_i^{(2)}\alpha M_\mathrm{f}\phi^2\rho_\mathrm{f} b_\mathrm{f}}{\rho A_i I_i^{(3)}}, \quad B_i^{(2)} = (\phi\rho_\mathrm{f}A_i)^2 \quad \text{and} \quad B^{(3)} = b_\mathrm{f}^2. \tag{53}$$

For small values of h, the term $B_i^{(2)}h^3$ is neglected compared to $B^{(3)}h$ and the added damping is inversely proportional to h. Equation (53) was derived in the framework of thin plate theory. When h tends to zero, the system should behave like a membrane and further investigation of this situation is required. However, this is beyond the scope of this study.

5. Experimental validation

This section presents validation results. The Mecanum Oberst test bench is used for the mechanical characterization of MPP. This system is based on the norm ASTM E756-05 [16] and is relevant for the measurement of the damping loss factor and the Young modulus. Since the test bench is standardized, the dimensions of the test system are imposed by the experimental setup introduced in Figure 7 and Figure 8(a). In order to easily associate the experimentally observed peaks with the proposed theory, the plates are chosen longer than wide. Thus, the mode shapes along y do not participate in the low frequency range. The plate section is considered as straight and rigid according to y and the previous model is simplified by using the Euler-Bernoulli theory. The microperforated steel plate of length L_x is

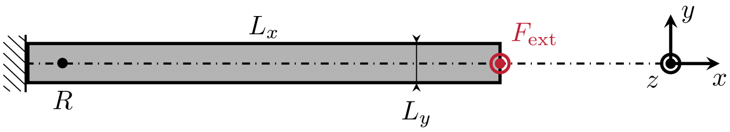

Figure 7: Steel plate used with the observation point R and the force excitation F_{ext} along z.

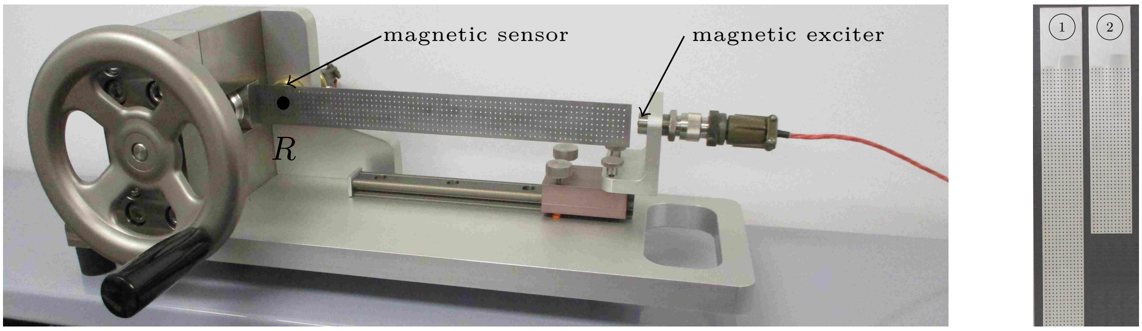

(a) (b)

Figure 8: Experimental setup in Figure 8(a) and MPPs used for damping characterization in Figure 8(b)

clamped at $x = 0$ and free at $x = L_x$ and free-free along y. A magnetic exciter placed at $x = L_x$ sends an exciting force of amplitude F_{ext}. The vibratory response of the plate saturated by air is measured with a magnetic sensor at the point R.

Two MPP configurations, presented in Figure 8(b), are used for validation purposes. The dimensions of the MPP ① are 298 mm × 30 mm × 0.87 mm while the dimensions of the MPP ② are 130 mm × 30 mm × 0.87 mm. Between these two configurations, the cross-section $L_y \times h$ and geometric parameters of the perforations are identical so that $\phi = 11\,\%$ and $d = 1\,\text{mm}$. Each MPP configuration corresponds to a non-perforated plate that acts as a reference. Several samples of each plate configuration were tested to quantify the error due to manufacturing and experimental errors. For each investigated microperforated plate, f_{c} is first calculated. The damping is assumed to be maximum for the mode i, when f_{c} is equal to the resonance frequency of mode i. To achieve this, the plate length can be adjusted in the range $L_x \in 95-300\,\text{mm}$ to fit the first or second frequency resonance of the MPP, with the damping characteristic frequency prescribed by d. In order to remain within the domain of sensor's validity, 50 Hz to 5000 Hz, and to maximize the damping which dominates at low frequencies on the mode at $f_i \approx f_{\text{c}} = 45\,\text{Hz}$, two lengths are considered to match the first or second natural mode of the MPP with f_{c}.

The mobility in dB for the tested plates with a comparison between analytical and experimental responses are presented in the following.

5.1. Maximum added damping on the first natural mode

In the case of the MPP ①, the analytical and experimental mobilities for the MPP are compared to those of the non-perforated plate in Figure 9. Measured Young modulus and the resonance frequency for the first plate mode are presented in Table 5 for MPP ① and the reference plate. Corresponding values obtained analytically are also given. The theoretical Young modulus is obtained from Equation (42)[4].

Experimental reference plate		**Experimental MPP ①**		**Theoretical MPP ①** (42)	
E (Mpa)	197037	E (Mpa)	149885	E (Mpa)	140487
f_1 (Hz)	51.1	f_1 (Hz)	37.3	f_1 (Hz)	37.2

Table 5: Measured and analytical Young's modulus and first resonance frequency for MPP ① and the corresponding experimentally obtained values for the reference plate. The theoretical Young's modulus is obtained in this table from the experimental Young's modulus of the reference plate and Equation (42).

For each resonance peaks, the gain in dB between measured MPP and plate reference can be obtain from

$$g = 20\log_{10}\left(\left|\frac{\dot{w}_{\text{s}}^{\text{ref}}(x_R, y_R, f_i)}{\dot{w}_{\text{s}}^{\text{MPP}}(x_R, y_R, f_i)}\right|\right), \tag{54}$$

---

[4] The Young modulus is f-dependent. The Young modulus sensitivity to frequency is not considered in Equation (42) and therefore in the analytical model.

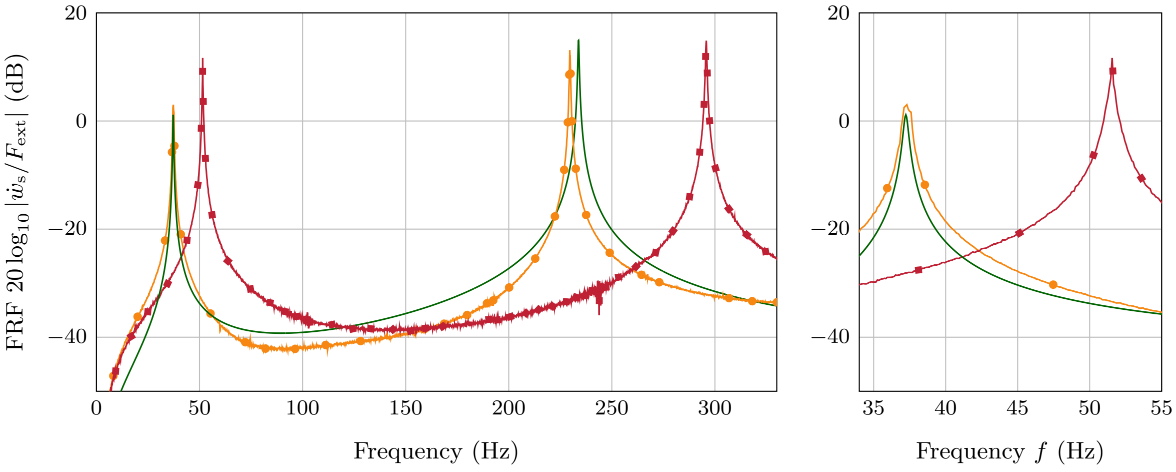

(a) (b)

Figure 9: Mobility of various clamped-free plate: (—■—) experimental non-perforated plate, (—●—) experimental MPP ①, (——) theoretical MPP ①. For theoretical and measured MPP ①, d is chosen to induce maximum damping for the first natural mode. The Figure 9(a) corresponds to the frequency response for the first two modes while the Figure 9(b) is a zoom on f_1, the first resonance mode. Perforation parameters are $d = 1\,\mathrm{mm}$ and $\phi = 11\,\%$.

where $\dot{w}_{\mathrm{s}}^{\mathrm{ref}}(x_R, y_R, f_i)$ and $\dot{w}_{\mathrm{s}}^{\mathrm{MPP}}(x_R, y_R, f_i)$ are respectively the solid velocity of the reference and the microperforated plate at the ith resonance frequency. The pair (x_R, y_R) is the coordinate of the observation point R represented in Figure 7.

From Figure 9, it can be observed that the microperforations increase the damping of the structure: for the tested MPP in Figure 9, the gain g is about 9 dB for f_1. For the other resonance peaks, the added damping is negligible. This is probably due to the fact that the natural frequencies of the MPP ① are relatively high for $i > 1$ and the added damping has more influence in the low frequency range.

5.2. Maximum added damping on the second natural mode

The mobility in dB for MPP ② is presented in Figure 10 with a comparison between analytical and experimental responses. In contrast to Figure 9, the peak corresponding to the first mode $f_1 \approx 8\,\mathrm{Hz}$ is not in the domain of sensor's validity. The values measured for this peak are therefore not considered. The gain of damping induced by the microperforations is about 5 dB for $f_2 \approx 46\,\mathrm{Hz}$. For higher frequency modes, the added damping is negligible. Frequencies responses presented in Figure 9(a) and Figure 10(a) are obtained with MPPs being same geometrical parameters (ϕ and d). Their comparison leads to the

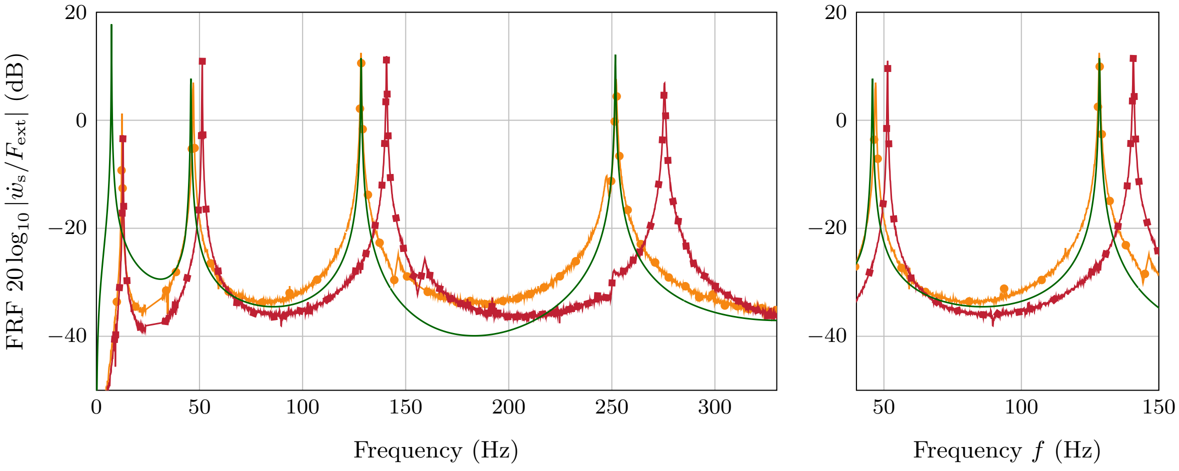

(a) (b)

Figure 10: Mobility of various clamped-free plate: (—■—) experimental non-perforated plate, (—●—) experimental MPP ②, (——) theoretical MPP ②. For theoretical and measured MPP ①, d is chosen to induce maximum damping for the second natural mode, f_2, and not for f_1 as in Figure 9. The Figure 10(a) corresponds to the frequency response for the first four modes while the Figure 10(b) is a zoom on the resonance mode f_2 and f_3. In order to respect the domain of sensor's validity, the first natural mode, which occurs at $f_1 \approx 8\,\mathrm{Hz}$ is not considered in the frequency response. Perforation parameters are $d = 1\,\mathrm{mm}$ and $\phi = 11\,\%$.

conclusion that regardless of the value of the frequency, the maximized added damping is greater for the first natural frequency. The added damping is specific to each plate and depends on its dimensions, its material and its boundary conditions. In the two frequency responses in Figure 9(a) and Figure 10(a), it can be noticed the presence of amplitude jumps, which may be caused by the experimental setup and its surrounding environment.

From the plate response presented in Figure 9 and Figure 10, each loss factor is characterized for each resonance mode i. The theoretical loss factor is compared to the one measured experimentally from the frequency responses depicted in Figure 10(a) and Figure 9(a). Each point is the average of several measurements. The variability of measurements is represented through error bars that correspond to one standard deviation of uncertainty. The results corresponding to MPP ② are presented in Figure 11(a), while those corresponding to the peaks for which $i > 1$ for MPP ① are given in Figure 11(b).

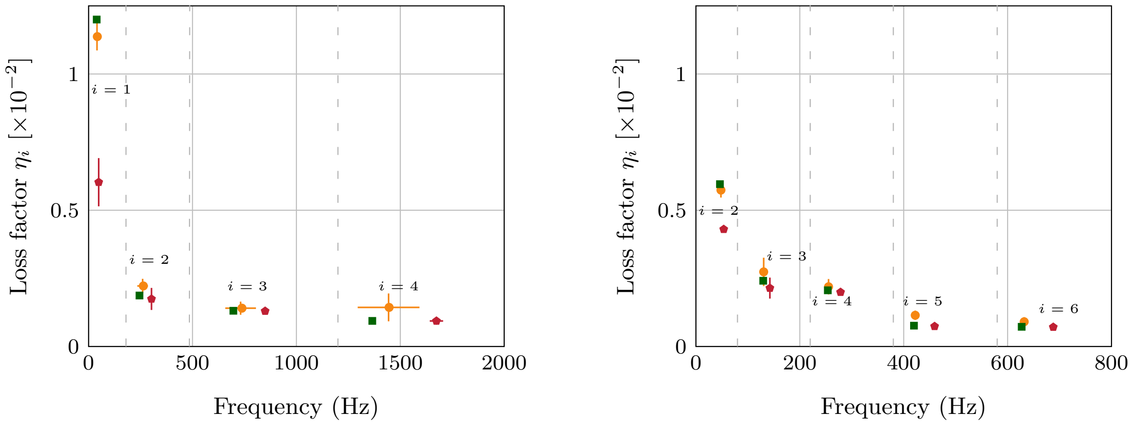

(a)

(b)

Figure 11: Measured loss factor for configurations ① in Figure 11(a) and ② in Figure 11(b) presented in this section: (—⬟—) the experimental non-perforated plate, (—●—) the experimental MPP, (—■—) the theoretical MPP. Each loss factor is determined for the ith mode that refers to the three colours. The damping is reached a maximum value at $f_i \approx f_c$ with $i = 1$ in Figure 11(a), $i = 2$ in Figure 11(b). In Figure 11(b), only modes in the domain of sensor's validity are represented. Perforation parameters are $d = 1\,\text{mm}$ and $\phi = 11\,\%$.

The damping added by the perforations increases the overall damping of the structure, especially in the low frequency range. For both the cases presented in Figure 11, the maximum damping is around 50 Hz, that is, on the first natural mode in Figure 11(a) and second natural mode in Figure 11(b). The overall damping increases by a factor of 1.9 in the case where the microperforations are adapted to induce maximum damping on the first natural mode. This factor is obtained for a given value of ϕ and would increase if ϕ were larger. In the case where the added damping is maximized at the second natural frequency, the increase factor is 1.3. In order to have the most efficient added damping, it is more interesting to maximize the damping on the first natural frequency mode and to increase ϕ. We conclude that the damping is non-linear with respect to frequency and mode. The damping added by the microperforations is more effective in the low frequency range. For moderate and high frequencies, the added damping is not significant, since the damping exhibited by the reference and microperforated plates are very similar.

Moreover, the comparison of the theoretical and experimental damping loss factors shows agreement with a maximum relative error of 15 % for modes below 330 Hz. The observed differences may be due to approximations and assumptions made about the elastic modulus, which is independent of frequency in the analytical model.

6. Conclusion

This paper describes the theoretical investigation and experimental validation of the vibration analysis of a finite size microperforated plate based on the extension of a vibration model for porous plates [21]. The porous plate vibration model is adapted to MPP using an approach based on the Johnson-Champoux-Allard model for rigid porous media. For an MPP with cylinder perforation with circular cross-section, all JCA parameters can be defined in terms of diameter and ratio of the perforations only. An effective tortuosity is added to consider the correction length induced by the MPP radiation in the surrounding fluid. Mechanical parameters (Young's modulus and density of the structure) are adapted to capture the effect of microperforations.

The proposed analytical model shows that the microperforations induce significant additional damping in the structure. This effect is validated by experimental measurements on microperforated plates. The observed added damping is induced by visco-thermal dissipation mechanisms in the microperforations combined with fluid-solid interactions. These effects are closely related to the thicknesses of the viscous and thermal boundary layers, which also are frequency dependent. Thus, the added damping reaches a maximum for a characteristic frequency that can only be defined as a function of the perforation diameter. Sensitivity analysis shows that the added damping is also effective over a significant frequency bandwidth, and is all the more important as the characteristic frequency is low. Moreover, the added damping is an increasing function of the perforation ratio and a decreasing function of the plate thickness. To maximize the effect of the added damping on the vibratory response of the structure to a given mode, it is advised to coincide the characteristic frequency with this mode frequency by adjusting the perforation diameter. Considering that the added damping effect is a low frequency effect, it is recommended to adjust the perforation diameter to induce maximum damping on the first MPP mode.

CRediT authorship contribution statement

Lucie Gallerand: Conceptualization, Methodology, Software, Validation, Writing - original draft, Writing - review & editing. **Mathias Legrand**: Conceptualization, Methodology, Supervision, Writing - original draft, review & editing. **Thomas Dupont**: Conceptualization, Methodology, Supervision, Resources, Funding acquisition, Writing - original draft, review & editing. **Philippe Leclaire**: Conceptualization, Methodology, Supervision, Writing - original draft, review & editing.

Supplementary material

The script used to perform the modal analysis presented in this article is available as a Jupyter NoteBook.

Acknowledgment

This work was supported by the Natural Sciences and Engineering Research Council of Canada (NSERC) and by Fonds de recherche du Québec - Nature et technologies (FRQNT).

A. Basis functions for particular boundary conditions

MPP with simply-supported boundary conditions

In the case of a simply-supported plate, Equation (20) becomes

$$\phi_m(x) = \sin(\Omega_m x) \quad \text{with} \quad \Omega_m = \frac{m\pi}{L_x}. \tag{A.1}$$

A similar expression holds in the y direction for the indices n.

MPP with clamped-free boundary conditions

In the case of an MPP clamped-free MPP, Equation (20) can be written as

$$\phi_m(x) = \cosh(\Omega_m x) - \cos(\Omega_m x) + c\sinh(\Omega_m x) + c\sin(\Omega_m x) \quad \text{with} \quad \Omega_m = \frac{(2m-1)\pi}{2L_x}, \tag{A.2}$$

and the constant c defined as follows

$$c = -\frac{\cosh(\Omega_m L_x) - \cos(\Omega_m L_x)}{\sinh(\Omega_m L_x) - \sin(\Omega_m L_x)}. \tag{A.3}$$

The basis function is thus expressed as $\Psi_{mn}(x, y) = \phi_m(x)\phi_n(y)$.

MPP with clamped boundary conditions

In the case of an MPP clamped on each edge, Equation (20) can be written as

$$\phi_m(x) = \cosh(\Omega_m x) + c\sinh(\Omega_m x) - c\sin(\Omega_m x) \quad \text{with} \quad \Omega_m = \frac{(2m+1)\pi}{2L_x}, \tag{A.4}$$

and the constant c defined as follows

$$c = \frac{-\cosh(\Omega_m L_x)}{\sinh(\Omega_m L_x) - (-1)^m}. \tag{A.5}$$

The basis function $\Psi_{mn}(x, y) = \phi_m(x)\phi_n(y)$ is thus expressed as

$$\begin{aligned}\Psi_{mn}(x, y) = {} & c^2\sin(\Omega_m x)\sin(\Omega_n y) + c^2\sinh(\Omega_m x)\sinh(\Omega_n y) - 2c^2\sinh(\Omega_m x)\sin(\Omega_n y) \\ & - 2c\sin(\Omega_m x)\cosh(\Omega_n y)) + 2c\sinh(\Omega_m x)\cosh(\Omega_n y) + \cosh(\Omega_m x)\cosh(\Omega_n y).\end{aligned} \tag{A.6}$$

B. Dissipative system with any damping

The following one-dof dissipative system is considered

$$\ddot{x}(t) + 2\zeta\omega\dot{x}(t) + \omega^2 x(t) = 0, \tag{B.1}$$

where ζ is the modal damping factor and ω the undamped frequency. The trivial equation $\dot{x}(t) - \dot{x}(t) = 0$ is joined to Equation (B.1) and the system

$$\ddot{x}(t) + 2\zeta\omega\dot{x}(t) + \omega^2 x(t) = 0, \tag{B.2a}$$
$$\dot{x}(t) - \dot{x}(t) = 0, \tag{B.2b}$$

is obtained and recast in the matrix form such that

$$\dot{\mathbf{z}}(t) = \mathbf{D}\mathbf{z}(t) \quad \text{where} \quad \mathbf{D} = \begin{bmatrix} 0 & 1 \\ -\omega^2 & -2\zeta\omega \end{bmatrix} \quad \text{and} \quad \mathbf{z}(t) = \begin{pmatrix} x(t) \\ \dot{x}(t) \end{pmatrix}. \tag{B.3}$$

To compute the response in autonomous regime, eigenvalues of the 2 dof system presented in Equation (B.3) are obtained in the complex conjugated form such that $\lambda = \beta \pm j\gamma$. The two-dimensional system of equation

$$\dot{z}(t) = \lambda z(t), \tag{B.4}$$

admits solutions of the form

$$z(t) = A\exp(\lambda t) \quad \Rightarrow \quad z(t) = A\exp(\beta t)\exp(\pm j\gamma t) \tag{B.5}$$

where A is a constant defined from initial conditions, $\beta = -\zeta\omega$ and $\gamma = \pm\omega\sqrt{1-\zeta^2}$.

References

[1] T. Adams. *Sound materials: A compendium of sound absorbing materials for architecture and design*. Frame Publishers, 2017. ISBN: 978-94-923-1153-5.

[2] N. Atalla and F. Sgard. Modeling of perforated plates and screens using rigid frame porous models. *Journal of Sound and Vibration*, 303:195–208, 2007. `hal-03623717`. `doi:10.1016/j.jsv.2007.01.012`.

[3] H. Aygun, K. Attenborough, and A. Cummings. Predicted effects of fluid loading on the vibration of elastic porous plates. *Acta Acustica united with Acustica*, 93:6, 2007. `hal-02293597`.

[4] R. Billard, G. Tissot, G. Gabard, and M. Versaevel. Numerical simulations of perforated plate liners: Analysis of the visco-thermal dissipation mechanisms. *Journal of the Acoustical Society of America*, 149(1):16–27, 2021. `doi:10.1121/10.0002973`.

[5] M.A. Biot. Theory of propagation of elastic waves in a fluid-saturated porous solid. I. Low-frequency range. *Journal of the Acoustical Society of America*, 28(2):168–178, 1956. `doi:10.1121/1.1908239`.

[6] M.A. Biot. Theory of propagation of elastic waves in a fluid-saturated porous solid. II. Higher frequency range. *Journal of the Acoustical Society of America*, 28(2):179–191, 1956. `doi:10.1121/1.1908241`.

[7] M.A. Biot and D.G. Willis. The elastic coefficients of the theory of consolidation. *Journal of Applied Mechanics*, pages 594–604, 1957. `doi:10.1115/1.4011606`.

[8] A.R. Boccaccini and Z. Fan. A new approach for the Young's modulus-porosity correlation of ceramic materials. *Ceramics International*, 23, 1997. `doi:10.1016/S0272-8842(96)00033-8`.

[9] T. Bravo, C. Maury, and C. Pinhède. Sound absorption and transmission through flexible micro-perforated panels backed by an air layer and a thin plate. *Journal of the Acoustical Society of America*, 131:3853–3863, 2012. `doi:10.1121/1.3701987`.

[10] T. Bravo, C. Maury, and C. Pinhède. Vibroacoustic properties of thin micro-perforated panel absorbers. *Journal of the Acoustical Society of America*, 132:789–798, 2012. `doi:10.1121/1.4733555`.

[11] E. Buckingham. On physically similar systems. Illustrations of the use of dimensional equations. *Physical Review*, 4(4):345–376, 1914. `hal-03623703`. `doi:10.1103/PhysRev.4.345`.

[12] F. Chevillotte. Controlling sound absorption by an upstream resistive layer. *Applied Acoustics*, 73:56–60, 2012. `hal-03620852`. `doi:10.1016/j.apacoust.2011.07.005`.

[13] P. Cobo and F. Simón. Multiple-layer microperforated panels as sound absorbers in buildings: A review. *Buildings*, 9(2):53, 2019. `doi:10.3390/buildings9020053`.

[14] M. Conesa, J.F. Sánchez Pérez, I. Alhama, and F. Alhama. On the nondimensionalization of coupled, nonlinear ordinary differential equations. *Nonlinear Dynamics*, 84(1):91–105, 2016. `doi:10.1007/s11071-015-2233-8`.

[15] T. Dupont, G. Pavic, and B. Laulagnet. Acoustic properties of lightweight micro-perforated plate systems. *Acta Acustica united with Acustica*, 89(2):201–212, 2003. `hal-03623544`.

[16] ASTM Designation: E756-05(2017). *Standard Test Method for Measuring Vibration-Damping Properties of Materials*. ASTM International, 2017. `ASTM E756-05(2017)`.

[17] U. Ingard. On the theory and design of acoustic resonators. *Journal of the Acoustical Society of America*, 25:1037–1061, 1953. `doi:10.1121/1.1907235`.

[18] T. Ito, A. Shintani, and C. Nakagawa. Vibration characteristics of a perforated plate immersed in fluid. In *Volume 8: Seismic Engineering*, pages 231–238, Toronto, Canada, 2012. ASME. `hal-03623685`. `doi:10.1115/PVP2012-78400`.

[19] L. Jaouen and F.-X. Bécot. Acoustical characterization of perforated facings. *Journal of the Acoustical Society of America*, 129:1400–1406, 2011. `doi:10.1121/1.3552887`.

[20] J. Kang and H.V. Fuchs. Predicting the absorption of open weave textiles and micro-perforated membranes backed by an air space. *Journal of Sound and Vibration*, 220(5):905–920, 1999. `doi:10.1006/jsvi.1998.1977`.

[21] P. Leclaire, K.V. Horoshenkov, and A. Cummings. Transverse vibration of a thin rectangular porous plate saturated by a fluid. *Journal of Sound and Vibration*, 247(1):1–18, 2001. `hal-01326042`. `doi:10.1006/jsvi.2001.3656`.

[22] P. Leclaire, K.V. Horoshenkov, M.J. Swift, and D.C. Hothersall. The vibrational response of a clamped rectangular porous plate. *Journal of Sound and Vibration*, 247(1):19–31, 2001. `hal-01326043`. `doi:10.1006/jsvi.2000.3657`.

[23] Y.Y. Lee and E.W.M. Lee. Widening the sound absorption bandwidths of flexible micro-perforated curved absorbers using structural and acoustic resonances. *International Journal of Mechanical Sciences*, 49(8):925–934, 2007. `doi:10.1016/j.ijmecsci.2007.01.008`.

[24] Y.Y. Lee, E.W.M. Lee, and C.F. Ng. Sound absorption of a finite flexible micro-perforated panel backed by an air cavity. *Journal of Sound and Vibration*, 287:227–243, 2005. `doi:10.1016/j.jsv.2004.11.024`.

[25] W. Liu, D.W. Herrin, and E. Bianchini. Diffuse field sound absorption of microperforated panels with special backings. *SAE International Journal of Vehicle Dynamics, Stability, and NVH*, 1(2):464–470, 2017. `doi:10.4271/2017-01-1876`.

[26] D.-Y. Maa. Microperforated-panel wideband absorbers. *Noise Control Engineering Journal*, 29(3):77, 1987. `doi:10.3397/1.2827694`.

[27] D.-Y. Maa. Potential of microperforated panel absorber. *Journal of the Acoustical Society of America*, 104:2861, 1997. `doi:10.1121/1.423870`.

[28] J.C. Maltbaek. Dimensional analysis and the theory of models. In *Further Engineering Dynamics*, pages 132–145. Macmillan Education UK, 1980. `doi:10.1007/978-1-349-16321-2_8`.

[29] F.P. Mechel. Helmholtz resonators with added porous absorbers. *Acta Acustica united with Acustica*, 80(3):268–279, 1994. `hal-03623739`.

[30] A.I. Mosa, A. Putra, R. Ramlan, I. Prasetiyo, and A. Esraa. Theoretical model of absorption coefficient of an inhomogeneous MPP absorber with multi-cavity depths. *Applied Acoustics*, 146:409–419, 2019. `doi:10.1016/j.apacoust.2018.11.002`.

[31] H. Nélisse, O. Beslin, and J. Nicolas. A generalized approach for the acoustic radiation from a baffled or unbaffled plate with arbitrary boundary conditions, immersed in a light or heavy fluid. *Journal of Sound and Vibration*, 211(2):207–225, 1998. `hal-03620855`. `doi:10.1006/jsvi.1997.1359`.

[32] S.-H. Park. A design method of micro-perforated panel absorber at high sound pressure environment in launcher fairings. *Journal of Sound and Vibration*, 332(3):521–535, 2013. `doi:10.1016/j.jsv.2012.09.015`.

[33] A. Putra, Y. M. Cheah, N. Muhammad, A. Rivai, and C. M. Wai. The effect of perforation on the dynamics of a flexible panel. *Advances in Acoustics and Vibration*, 2014:1–17, 2014. `doi:10.1155/2014/526045`.

[34] A Putra, A. Rivai, Wai C. Mun, and N Muhammad. Preliminary Investigation on the Perforated Panel Mobility Using Finite Element Method. *Applied Mechanics and Materials*, 471:341–346, 2013. `doi:10.4028/www.scientific.net/AMM.471.341`.

[35] A. Putra and D.J. Thompson. Sound radiation from perforated plates. *Journal of Sound and Vibration*, 329(20):4227–4250, 2010. `doi:10.1016/j.jsv.2010.04.020`.

[36] M. Régniez. *Amortissement des vibrations de réflecteur d'antenne de satellite par micro-perforations (Vibration damping of satellite antenna reflector by micro-perforations)*. PhD thesis, Université du Maine, 2015. `tel-01163673`.

[37] D. Takahashi and M. Tanaka. Flexural vibration of perforated plates and porous elastic materials under acoustic loading. *Journal of the Acoustical Society of America*, 112(4):1456–1464, 2002. `doi:10.1121/1.1497624`.

[38] D.D. Theodorakopoulos and D.E. Beskos. Flexural vibrations of poroelastic plates. *Acta Mechanica*, 103(1-4):191–203, 1994. `doi:10.1007/BF01180226`.

[39] J.C. Wang. Young's modulus of porous materials: Part 1 theoretical derivation of modulus-porosity correlation. *Journal of Materials Science*, 19, 1984. `doi:10.1007/BF00540451`.

[40] L. Wang and T. Wang. Investigation of the effect of perforated sheath on thermal-flow characteristics over a gas turbine reverse-flow combustor—Part 2: Computational analysis. *Journal of Thermal Science and Engineering Applications*, 12(4), 2019. `doi:10.1115/1.4045391`.

[41] M.Q. Wu. Micro-perforated panels for duct silencing. *Noise Control Engineering Journal*, 45(2):69–77, 1997. `doi:10.3397/1.2828428`.